A Passivity-Based Small-Signal DEF Analysis for Low-Frequency Oscillation Source Characterization of VSC-HVdc

Kaustav Chatterjee, *Member, IEEE,* Sayan Samanta, *Student Member, IEEE,* and Nilanjan Ray Chaudhuri, *Senior Member, IEEE*

***Abstract*—In bulk power systems, detecting the sources of low-frequency oscillations can be challenging. The energy-based approaches for oscillation source localization are known to have better accuracy compared to others. The dissipating energy flow (DEF) method is one such approach with notable success in localizing real-world oscillation cases. While the mathematical justifications for the method's characterization of a device as an oscillation source (or sink) is well-exposed for synchronous generators and standalone inverters, no insights have been developed for power-electronics-interfaced dc transmission systems. To fill this gap, this paper presents a theoretical analysis of the DEF in a voltage source converter-based high voltage direct current (VSC-HVdc) system. Passivity-based analysis is performed to explain why a VSC-HVdc system, operating at unity power factor, with the commonly used control strategy involving constant real power control, dc-link voltage control, and ac voltage–reactive power droop control is a source of oscillation energy. Supporting case studies are performed on the IEEE 4-machine and IEEE 16-machine 68-bus test systems.**

***Index Terms*—Low-frequency oscillations, dissipating energy flow, oscillation source, passivity, VSC-HVdc.**

I. Introduction

In the monitoring of bulk power systems it is common to observe low-frequency electromechanical oscillations (typically, $0.2 - 2$ Hz) in the system variables. The oscillatory behaviour can be attributed to the transient energy associated with the system's poorly-damped natural modes and/or the external perturbations [1], [2]. These oscillations, if sustained, can impose serious threat to system stability and security [3]. Once detected, as a first-step in mitigating these, it is important to localize their sources in the grid [4]. For forced oscillations (FOs), defining their source is relatively easier. The component 'generating' the oscillation by means of external perturbations, unambiguously, is the source. However, for sustained oscillations from poorly-damped natural modes, the source characterization is more complicated [5]. There could be more than one element, which depending on their control designs, may negatively impact the damping of a mode by shifting its eigenvalue to the right. Such elements with negative damping contributions could be characterized as sources [4].

K. Chatterjee is with the Pacific Northwest National Laboratory, Richland, WA 99354, USA (email: kaustav.chatterjee@pnnl.gov).

S. Samanta and N. R. Chaudhuri are with the Department of Electrical Engineering, Pennsylvania State University, University Park, PA 16802, USA (e-mail: sps6260@psu.edu, nuc88@psu.edu).

Financial support from NSF grants under awards CNS 1739206 and ECCS 1656983 is gratefully acknowledged.

Over the years, several methods for oscillation source localization have been proposed [6], [7]. These may be broadly classified into following groups: (a) mode-shape based methods [8]–[10], (b) damping torque based methods [11], (c) dissipating energy based methods [4], [12], [13], (d) equivalent circuit based methods [14], [15], and (e) machine learning and other data-driven methods [5], [16]. Detailed comparison of these methods with respect to their their strengths and limitations can be found in [6], [7].

In this paper, we focus our attention to the dissipating energy flow (DEF)-method, which has shown promising results on 1000+ real-world oscillation cases [17]. The method, as originally proposed in [12], calculates the average transient energy dissipation (also referred to as, 'oscillation energy dissipation') in a device leveraging the Lyapunov-like energy functions developed in [18]. In the DEF method, a source is defined as a system component which aids in sustaining the oscillation by supplying transient energy, either directly – as in the case of forced oscillations, or by deteriorating system damping – as in the case of poorly-damped modes [4]. The theoretical deductions leading to the method assume a lossless transmission network and constant power loads [12], [19]. In [4], [17], [20], [21] the impact of these assumptions on the accuracy of the method are carefully examined. These studies concluded that, impacts of line resistances on the DEF patterns are marginal [4], [17]. The studies further concluded that the deviation of the load characteristics from constant power to constant impedance may obfuscate the energy flow patterns in the network but their impact on the accuracy of the source localization are less likely to be critical [4], [17]. In [22], authors identified a few cases where the DEF method might fail. Notwithstanding these limitations, the success of the method is widely recognized, as is evident from its successful adoption in the oscillation management system of ISO-NE [17]. In the recent years, extensions and improvements on the existing DEF method have also been studied – notable of these are [4], [23]–[26].

The theoretical analysis of the DEF-method and its connection to damping torque analysis is well-studied for synchronous generators [19], [27], [28]. However other network components, especially the power electronics-interfaced active transmission devices remains largely unexplored in this context. While it is true that, in most cases the oscillation source is in a generator's control systems (e.g., exciters, stabilizers, governors, or turbine-boiler systems) [17], many a time the

source has also been detected outside the generator in power electronics-interfaced transmission systems. For example, on May 23, 2018, sustained 0.4 Hz oscillations were observed at multiple locations in the Western Electricity Coordinating Council (WECC) system and the source of these oscillations was identified in the controls of the Pacific DC Intertie HVdc system [17]. In [26], a new DEF method is derived for detecting oscillation sources in grid-following inverters. In [21], authors use the passivity theory to offer an insightful interpretation of the DEF. The analysis is then applied to grid-forming converters under droop control with a stiff dc source. In [29], the DEF-based oscillation source/sink behavior of thyristor-controlled series capacitors (TCSCs) and static synchronous compensators (STATCOMs) and their controls are studied. No insights, however, have been developed regarding the DEFs for HVdc transmission systems. In our understanding, compared to a single converter system, the analysis of a HVdc system is more complex due to the coupling between transient energy functions of the rectifier- and inverter-end converters. The coupling stems from the dependence of real powers injected by the two converter terminals due to power balance. In addition, due to the interconnected nature of an ac system corresponding reactive power injections can also be dependent if the ac voltage is controlled at the respective terminals.

Thus motivated, in this paper we present the analysis of DEF in VSC-HVdc systems for low-frequency electromechanical oscillations. The operating conditions and controls leading to the source characterization of the device are highlighted. Drawing insights from the notions of passivity and positive realness, the paper presents analytical derivations explaining why a VSC-HVdc system with the conventional control strategy (see for example, [30]) involving real power control, reactive power-ac voltage droop, and dc voltage control is a source of oscillation energy flow.

The paper is organized as follows. In Section II, the VSC-HVdc system with the rectifier- and inverter-end controls is described. In Section III, the preliminaries on DEF, passivity, and the connections between them are introduced. Thereafter, in Section IV, main result of the paper explaining the oscillation-source behaviour of the system in Section II is presented. The case studies on the IEEE test systems are discussed in Section V followed by conclusions in Section VI.

II. System Description

Consider a point-to-point HVdc system connecting two ends of a synchronous ac system, as shown in Fig. 1. In addition to the HVdc link, the rectifier and the inverter bus are also connected via the ac network. The HVdc link, in study, is detailed in Fig. 2 with all symbols having their usual meanings, as described below.

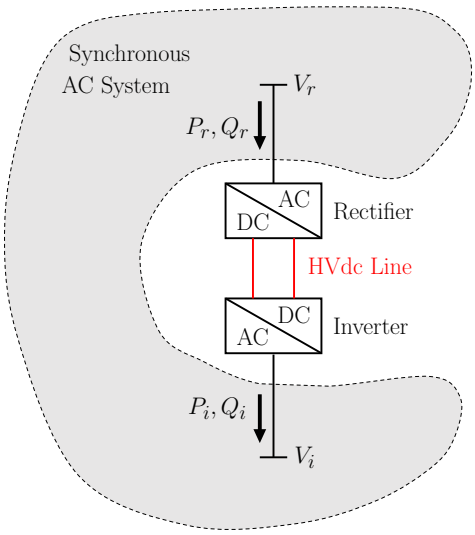

Fig. 1: Schematic of an HVdc system routing power between two points of a synchronous ac system.

Notations: V_r, I_r, P_r, Q_r, and V_i, I_i, P_i, Q_i are respectively, the ac-side voltage, current, and the real and reactive powers flowing into the device at the rectifier-end, and flowing out of the device at the inverter-end. C_r, C_i, V_{dc_r}, and V_{dc_i} are respectively, the rectifier- and inverter-end dc-capacitances and dc-bus voltages, i_{dc} is the dc-link current, and R is the dc-link resistance. The steady-state quantities are denoted by superscript 0 and the perturbations from the steady-state by prefix Δ, i.e., any variable $x = x^0 + \Delta x$.

The following phasor representations are considered in the rectifier's and inverter's $d-q$ reference frames determined respectively by their phase-locked-loops (PLLs),

$$\begin{aligned} \vec{V}_r &= V_{d_r} + jV_{q_r}, & \vec{I}_r &= I_{d_r} + jI_{q_r}, \\ \vec{V}_i &= V_{d_i} + jV_{q_i}, \quad \text{and} & \vec{I}_i &= I_{d_i} + jI_{q_i}. \end{aligned} \tag{1}$$

PLLs ensure that in steady state, the d-axes align with respective bus voltage phasors. Typically, this is achieved by driving the q-component of voltage vector to zero using a closed-loop tracking control. Hence, $V_r^0 = V_{d_r}^0$ and $V_{q_r}^0 = 0$. Following which, the linearization of $V_r^2 = V_{d_r}^2 + V_{q_r}^2$ around the steady-state, yields

$$2V_r^0 \Delta V_r = 2V_{d_r}^0 \Delta V_{d_r} + 2V_{q_r}^0 \Delta V_{q_r} \implies \Delta V_r = \Delta V_{d_r}. \tag{2}$$

Similarly, for the inverter-end we have $\Delta V_i = \Delta V_{d_i}$.

Please note that, in the interest of simplifying the mathematical analysis, the dynamics the PLL is not explicitly modeled

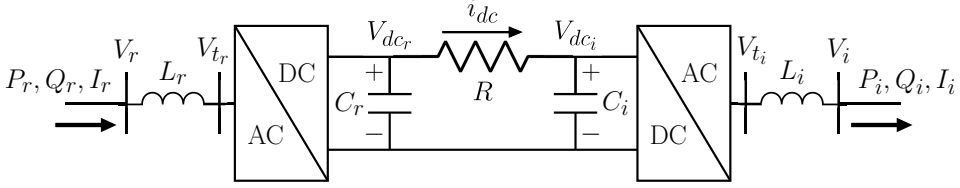

Fig. 2: Schematic of the VSC-HVdc system under study.

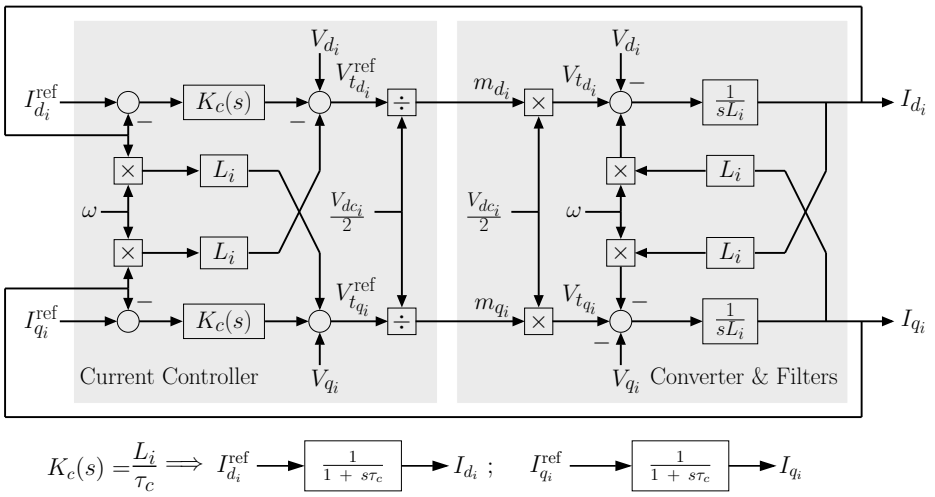

Fig. 3: Inner current loops (only shown for the inverter-end) and their simplification.

in the DEF equations[1]. The PLL's effect however, is modeled by considering nonzero ΔV_{q_i} and ΔV_{d_i} during transients. Also note, such a simplified representation of PLL is only limited to the analytical deductions and the proofs of the theorems. The numerical verification (see, the case studies in Section (V)) of the theorems consider a detailed model of PLL as shown in Fig. 4.

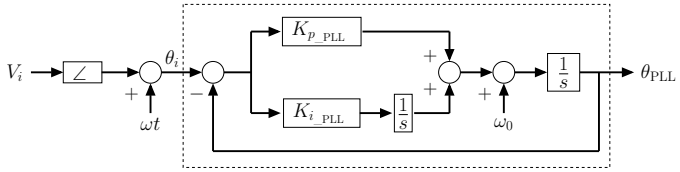

Fig. 4: The model of the PLL used in the case studies in Section V.

The real and reactive powers at the rectifier-end are expressed as, $P_r = V_{d_r} I_{d_r} + V_{q_r} I_{q_r}$ and $Q_r = V_{q_r} I_{d_r} - V_{d_r} I_{q_r}$ [31]. Similarly, $P_i = V_{d_i} I_{d_i} + V_{q_i} I_{q_i}$ and $Q_i = V_{q_i} I_{d_i} - V_{d_i} I_{q_i}$ [31]. In steady state, both rectifier and inverter operates at unity power factor, implying, $Q_r^0 = Q_i^0 = 0$. Operation under unity power factor leads to minimum ac current flowing through the HVdc terminals, thereby minimizing losses. Another practical reason behind unity power factor operation is to ensure dynamic reactive power reserve for voltage support under contingencies akin to a static var compensator, as mentioned in [32, pp. 44]. The real power deviations, obtained from linearization[2], can be expressed as,

$$\Delta P_r = V_{d_r}^0 \Delta I_{d_r} + I_{d_r}^0 \Delta V_{d_r} = V_r^0 \Delta I_{d_r} + I_{d_r}^0 \Delta V_{d_r}, \quad (3)$$

$$\text{and } \Delta P_i = V_{d_i}^0 \Delta I_{d_i} + I_{d_i}^0 \Delta V_{d_i} = V_i^0 \Delta I_{d_i} + I_{d_i}^0 \Delta V_{d_i}. \quad (4)$$

The inner current control loops reject the measurable disturbances by using feedforward control signals I_{d_i}, I_{q_i}, V_{d_i}, V_{q_i}, and $\frac{V_{dc_i}}{2}$ as shown in Fig 3. Moreover, the controller $K_c(s)$ is designed to be equal to $\frac{L_i}{\tau_c}$, where τ_c is the desired time-constant of the closed-loop step response [31]. Upon simplification we can write,

$$\frac{I_{d_r}}{I_{d_r}^{\text{ref}}} = \frac{I_{q_r}}{I_{q_r}^{\text{ref}}} = \frac{I_{d_i}}{I_{d_i}^{\text{ref}}} = \frac{I_{q_i}}{I_{q_i}^{\text{ref}}} = \frac{1}{1+s\tau_c}. \quad (5)$$

In the control of real and reactive powers, following strategies are considered:

1) *Rectifier-end real power control* (see, Fig. 5):

$$\begin{aligned} I_{d_r}^{\text{ref}} &= K_r(s)(P_r^{\text{ref}} - P_r) \\ \implies I_{d_r} &= \frac{K_r(s)}{1+s\tau_c}(P_r^{\text{ref}} - P_r) \end{aligned} \quad (6)$$

where $P_r^{\text{ref}} = P_r^0$,

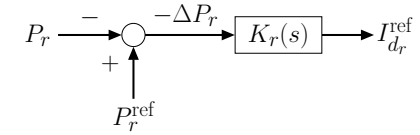

Fig. 5: Rectifier-end real power control in the VSC-HVdc system.

2) *Rectifier-end ac voltage–reactive power droop control* (see, Fig. 6):

$$\begin{aligned} I_{q_r}^{\text{ref}} &= \frac{V_{q_r} I_{d_r}^{\text{ref}} - Q_r^{\text{ref}}}{V_{d_r}} \\ \implies I_{q_r} &= \frac{V_{q_r} I_{d_r}}{V_{d_r}} - \frac{1}{1+s\tau_c}\frac{Q_r^{\text{ref}}}{V_{d_r}} \end{aligned} \quad (7)$$

where $Q_r^{\text{ref}} = Q_r^0 + \Delta Q_r^{\text{ref}}$ and $\Delta Q_r^{\text{ref}} = K_{q_r} \Delta V_r = K_{q_r} \Delta V_{d_r}$,

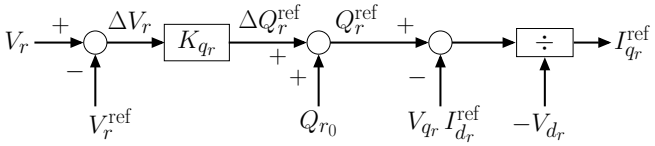

Fig. 6: Rectifier-end ac voltage–reactive power droop control in the VSC-HVdc system.

[1] PLL dynamics is much faster compared to the electromechanical transients analysed in this paper. Therefore, it is reasonable to assume PLLs synchronized while modeling the low-frequency oscillations in the DEF equations.

[2] Recall, $V_{d_r}^0 = V_r^0$ and $V_{q_r}^0 = 0$, therefore, $Q_r^0 = V_{q_r}^0 I_{d_r}^0 - V_{d_r}^0 I_{q_r}^0 = 0 \implies I_{q_r}^0 = 0$. Similarly, $I_{q_i}^0 = 0$.

3) *Inverter-end dc-bus voltage control* (see, Fig. 7):

$$\begin{aligned} I_{d_i}^{\text{ref}} &= \frac{K_v(s)}{V_{d_i}}\Big(V_{dc_i}^2 - (V_{dc_i}^{\text{ref}})^2\Big) \\ \implies I_{d_i} &= \frac{1}{1+s\tau_c}\frac{K_v(s)}{V_{d_i}}\Big(V_{dc_i}^2 - (V_{dc_i}^{\text{ref}})^2\Big), \end{aligned} \tag{8}$$

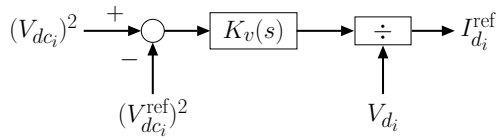

Fig. 7: Inverter-end dc-bus voltage control in the VSC-HVdc system.

4) *Inverter-end ac voltage–reactive power droop control* (see, Fig. 9):

$$\begin{aligned} I_{q_i}^{\text{ref}} &= \frac{V_{q_i} I_{d_i}^{\text{ref}} - Q_i^{\text{ref}}}{V_{d_i}} \\ \implies I_{q_i} &= \frac{V_{q_i} I_{d_i}}{V_{d_i}} - \frac{1}{1+s\tau_c}\frac{Q_i^{\text{ref}}}{V_{d_i}} \end{aligned} \tag{9}$$

where, $Q_i^{\text{ref}} = Q_i^0 + \Delta Q_i^{\text{ref}}$ and $\Delta Q_i^{\text{ref}} = K_{q_i}\Delta V_i = K_{q_i}\Delta V_{d_i}$.

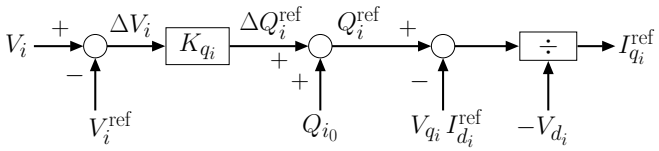

Fig. 8: Inverter-end ac voltage–reactive power droop control in the VSC-HVdc system.

Additionally, the sensor delays in the feedback loops and the resistances in the filter inductors are neglected.

III. Preliminaries on DEF and Passivity

Definition 1. [12] The DEF into an element $\mathcal{E}$ connected to the power network at bus k, denoted by $W_{\mathcal{E}}^D$, is expressed as

$$W_{\mathcal{E}}^D = \int \Im\{\Delta\vec{I}_{inj}^{*}\ d\Delta\vec{V}_k\}$$

where $\Delta\vec{V}_k$ and $\Delta\vec{I}_{inj}$ are respectively, the small-signal phasors of the perturbations in the voltage at bus k and the current injected into $\mathcal{E}$ from the network, and $\Im(\cdot)$ denotes the imaginary part of a complex number . □

Building on this, for the VSC-HVdc system described in Section II, total DEF flowing in (adding the rectifier and inverter contributions), denoted by W_{HVdc}^D, is expressed as

$$\begin{aligned} W_{\text{HVdc}}^D &= \int \Im\{\Delta\vec{I_r}^{*} d\Delta\vec{V_r}\} - \int \Im\{\Delta\vec{I_i}^{*} d\Delta\vec{V_i}\} \\ &= \int (\Delta I_{d_r} d\Delta V_{q_r} - \Delta I_{q_r} d\Delta V_{d_r} \\ &\qquad - \Delta I_{d_i} d\Delta V_{q_i} + \Delta I_{q_i} d\Delta V_{d_i}). \end{aligned} \tag{10}$$

We define

$$y^T := \begin{bmatrix} \Delta I_{d_r} & \Delta I_{q_r} & \Delta I_{d_i} & \Delta I_{q_i} \end{bmatrix}, \tag{11}$$

and

$$u^T := \begin{bmatrix} \Delta\dot{V}_{q_r} & -\Delta\dot{V}_{d_r} & -\Delta\dot{V}_{q_i} & \Delta\dot{V}_{d_i} \end{bmatrix}. \tag{12}$$

Following which, we may write

$$W_{\text{HVdc}}^D(t_1) = \int_0^{t_1} u^T y\ dt. \tag{13}$$

Definition 2. [12] Element $\mathcal{E}$ is called a sink (source) of oscillation energy if and only if the average slope of the DEF into $\mathcal{E}$ over a cycle $\mathcal{T}$, is positive (negative). □

In other words, the VSC-HVdc system is a sink of oscillation energy if

$$\dot{W}_{\text{HVdc}}^D = \frac{1}{\mathcal{T}}\int_0^{\mathcal{T}} u^T y\ dt > 0 \tag{14}$$

and a source if $\dot{W}_{\text{HVdc}}^D < 0$.

Next, consider the linearized representation of the system in Section II, denoted by Ω (see, (15)), with u and v as the input and output, respectively.

$$\Omega: \quad \dot{x} = Ax + Bu; \qquad y = Cx + Du \tag{15}$$

From [33, Def. 6.3], Ω *is said to be passive with respect to the supply rate* $u^T y$ *if there exists a continuously differentiable positive semidefinite storage function* $S(x)$ *such that* $u^T y \geqslant \dot{S}(x)$. Passivity of Ω implies, between any two instants, the energy flowing in is greater than the change in system's energy storage (see, (16)). Therefore,

$$W_{\text{HVdc}}^D(\mathcal{T}) = \int_0^{\mathcal{T}} u^T y\ dt\ \geqslant\ S(x(\mathcal{T}))\ -\ S(x(0)). \tag{16}$$

Since $S(x(0)) = 0$ and $S(x(\mathcal{T})) \geqslant 0$, we may write (16) as,

$$W_{\text{HVdc}}^D(\mathcal{T}) = \int_0^{\mathcal{T}} u^T y\ dt\ \geqslant\ 0. \tag{17}$$

Therefore, passivity of Ω with respect to the supply rate $u^T y$ implies, $\int u^T y\ dt \geqslant 0$. Further, from [34, Lemma 10] we know that the system is passive *if and only if* the corresponding transfer function matrix $G(s)$, between the input-output pair u and y, is *positive real*. Following which, from Def. 2, it may be said that the positive realness of $G(s)$ implies the underlying system is a sink[3] and its negation indicates the system is a source of oscillation energy. A summary of this is presented in Fig. 9.

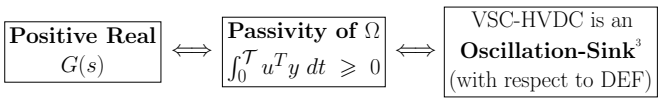

Fig. 9: Equivalence of positive realness, passivity, and the oscillation-sink behavior with respect to DEF.

To that end, in this paper, we derive the expression of $G(s)$ for the VSC-HVdc system described in Section II. Thereafter, we check if $G(s)$ satisfies the conditions for positive realness, as defined in [33, Def. 6.4]. This is presented in Section IV next.

[3] or neither a sink nor a source, i.e., *lossless*, for the $\int u^T y\ dt = 0$ case

At this point it is worth highlighting that, although the analysis in this paper focuses on the linearized small-signal representation of the HVdc system, the concepts of passivity and positive realness are stronger and can be applied to the analysis of the nonlinear system. The linearized representation, without much loss of accuracy, adequately captures the ambient dynamics of the system and is reasonable to understand the source/sink behavior in this context. Furthermore, this renders the analysis tractable.

IV. Passivity-based Analysis of DEF

A. Deriving the Transfer Function Matrix

Consider the VSC-HVdc system desribed in Section II. Linearizing (5), and thereafter, substituting (3) we obtain

$$\Big(V_r^0 + \frac{1+s\tau_c}{K_r(s)}\Big)\Delta I_{d_r} = -I_{d_r}^0 \Delta V_{d_r}. \tag{18}$$

Defining $\alpha_2(s) := V_r^0 + (1+s\tau_c)/K_r(s)$, (18) may be re-written as

$$\alpha_2(s)\ \Delta I_{d_r} = -I_{d_r}^0 \Delta V_{d_r}. \tag{19}$$

Similarly, linearizing[1] (6) , we obtain

$$V_r^0 \Delta I_{q_r} = -\frac{K_{q_r}}{1+s\tau_c}\Delta V_{d_r} \ + \ I_{d_r}^0 \Delta V_{q_r}. \tag{20}$$

Next, for the dc-side, the following power balance equations can be written at the rectifier- and inverter-end dc-buses,

$$P_r = \frac{1}{2}C_r\frac{dV_{dc_r}^2}{dt} \ + \ i_{dc}^2 R \ + \ \frac{1}{2}C_i\frac{dV_{dc_i}^2}{dt} \ + \ P_i, \tag{21}$$

$$i_{dc} = C_i\frac{dV_{dc_i}}{dt} + \frac{P_i}{V_{dc_i}}, \tag{22}$$

$$\frac{P_r}{V_{dc_r}} = C_r\frac{dV_{dc_r}}{dt} + i_{dc}. \tag{23}$$

Linearizing[4] (21) $-$ (23) and taking Laplace transform, we obtain[5]

$$\Delta P_r = \ sC_rV_{dc_r}^0\Delta V_{dc_r} + 2i_{dc}^0\Delta i_{dc}R + sC_iV_{dc_i}^0\Delta V_{dc_i} + \Delta P_i, \tag{24}$$

$$\Delta i_{dc} = \frac{1}{V_{dc_i}^0}\Big(sC_iV_{dc_i}^0\Delta V_{dc_i} \ + \ \Delta P_i \ - \ i_{dc}^0\Delta V_{dc_i}\Big), \tag{25}$$

$$\Delta P_r = sC_rV_{dc_r}^0\Delta V_{dc_r} + i_{dc}^0\Delta V_{dc_r} + V_{dc_r}^0\Delta i_{dc}. \tag{26}$$

Further, substituting (25) in (26), we arrive at $\Delta V_{dc_r} =$

$$=\frac{1}{sC_rV_{dc_r}^0 + i_{dc}^0}\Big(\Delta P_r - \frac{V_{dc_r}^0}{V_{dc_i}^0}(sC_iV_{dc_i}^0 - i_{dc}^0)\Delta V_{dc_i} - \frac{V_{dc_r}^0}{V_{dc_i}^0}\Delta P_i\Big). \tag{27}$$

Next, we linearize the control law in (8) to obtain

$$\Delta V_{dc_i} = \frac{1+s\tau_c}{2\ V_{dc_i}^0 K_v(s)}(V_{d_i}^0\Delta I_{d_i} + I_{d_i}^0\Delta V_{d_i}). \tag{28}$$

[4] Linearization of $x = \frac{1}{2}C\frac{d}{dt}V^2 \implies \Delta x = C(V^0+\Delta V)\Delta\dot{V}$. For small perturbations, approximated as, $\Delta x = CV^0\Delta\dot{V}$.

[5] For notational simplicity, the time-domain variables in (21) $-$ (23) and their corresponding s-domain mappings in (24) $-$ (26) and everywhere else in the paper are denoted by same symbols.

Substituting these expressions of ΔV_{dc_r}, ΔV_{dc_i}, and Δi_{dc} into (24), we get

$$f_1(s)\Delta P_r = f_2(s)\Delta P_i + f_3(s)(V_{d_i}^0\Delta I_{d_i} + I_{d_i}^0\Delta V_{d_i}). \tag{29}$$

For the detailed expressions of $f_1(s)$, $f_2(s)$, and $f_3(s)$, see Appendix A. The expression in (29) can be simplified by substituting the linearized expressions of ΔP_r and ΔP_i (from (3) and (4)) into it. Doing so, we get

$$V_r^0\Delta I_{d_r} - \alpha_1(s)V_i^0\Delta I_{d_i} = -I_{d_r}^0\Delta V_{d_r} + \alpha_1(s)I_{d_i}^0\Delta V_{d_i} \tag{30}$$

where, $\alpha_1(s) := (f_2(s)+f_3(s))/f_1(s)$.

Finally, linearizing (9), we have

$$V_i^0\Delta I_{q_i} = -\frac{K_{q_i}}{1+s\tau_c}\Delta V_{d_i} + I_{d_i}^0\Delta V_{q_i}. \tag{31}$$

Equations (19), (20), (30), and (31) along with the definitions (11) and (12) can be combined in a matrix representation as shown in (32) below

$$\mathcal{M}(s)\ y = \mathcal{N}(s)\ v \tag{32}$$

where,

$$\mathcal{M}(s) = \begin{bmatrix} \alpha_2(s) & 0 & 0 & 0 \\ 0 & V_r^0 & 0 & 0 \\ V_r^0 & 0 & -\alpha_1(s)V_i^0 & 0 \\ 0 & 0 & 0 & V_i^0 \end{bmatrix}, \tag{33}$$

$$\mathcal{N}(s) = \begin{bmatrix} -I_{d_r}^0 & 0 & 0 & 0 \\ -\frac{K_{q_r}}{1+s\tau_c} & I_{d_r}^0 & 0 & 0 \\ -I_{d_r}^0 & 0 & \alpha_1(s)I_{d_i}^0 & 0 \\ 0 & 0 & -\frac{K_{q_i}}{1+s\tau_c} & I_{d_i}^0 \end{bmatrix}, \tag{34}$$

and

$$v = \begin{bmatrix} \Delta V_{d_r} & \Delta V_{q_r} & \Delta V_{d_i} & \Delta V_{q_i} \end{bmatrix}. \tag{35}$$

Also, note that

$$v = \begin{bmatrix} 0 & -\frac{1}{s} & 0 & 0 \\ \frac{1}{s} & 0 & 0 & 0 \\ 0 & 0 & 0 & \frac{1}{s} \\ 0 & 0 & -\frac{1}{s} & 0 \end{bmatrix} u := \mathcal{P}(s)\ u. \tag{36}$$

Substituting this, (32) can be written as

$$y = G(s)\ u \tag{37}$$

where,

$$G(s) = \{\mathcal{M}(s)\}^{-1}\mathcal{N}(s)\ \mathcal{P}(s)$$
$$= \begin{bmatrix} 0 & \frac{I^0_{d_r}}{s\ \alpha_2(s)} & 0 & 0 \\ \frac{I^0_{d_r}}{s\ V^0_r} & \frac{K_{q_r}}{s\ (1+s\tau_c)\ V^0_r} & 0 & 0 \\ 0 & \frac{-I^0_{d_r}}{s\ \alpha_1(s) V^0_i}\left(1-\frac{V^0_r}{\alpha_2(s)}\right) & 0 & \frac{-I^0_{d_i}}{s\ V^0_i} \\ 0 & 0 & \frac{-I^0_{d_i}}{s\ V^0_i} & \frac{-K_{q_i}}{s\ (1+s\tau_c)\ V^0_i} \end{bmatrix}. \tag{38}$$

The detailed derivation of $G(s)$ is presented in Appendix B.

B. Positive Realness of the Transfer Function Matrix

Lemma 1. *$G(s)$ is not positive real.*

Proof. We prove this by contradiction. First, assume $G(s)$ derived in (38) is positive real. Next, define $L(j\omega) := G(j\omega) + G^T(-j\omega)$, where superscript T denotes the transpose operator. Since $G(s)$ is assumed positive real, from the definition [33, Def. 6.4], this implies $\forall\ \omega \neq 0$, $L(j\omega)$ is positive semidefinite.

Observe that from the expression of $G(s)$, the structure of $L(j\omega)$ can be inferred as

$$L(j\omega) \triangleq \begin{bmatrix} 0 & \ell_{12} & 0 & 0 \\ \ell^*_{12} & \ell_{22} & \ell_{23} & 0 \\ 0 & \ell^*_{23} & 0 & 0 \\ 0 & 0 & 0 & \ell_{44} \end{bmatrix}. \tag{39}$$

The characteristic equation of $L(j\omega)$ is

$$\lambda\Big\{\lambda^3 - \lambda^2(\ell_{22}+\ell_{44}) + \lambda(\ell_{22}\ell_{44} - |\ell_{12}|^2 - |\ell_{23}|^2) + \ell_{44}|\ell_{23}|^2 + \ell_{44}|\ell_{12}|^2\Big\} = 0. \tag{40}$$

Since, in accordance with our assumption, $L(j\omega)$ is positive semidefinite, all four eigenvalues (λ_i, for $i = 1, \ldots 4$) of $L(j\omega)$ should be non-negative. As seen from (40), one of the eigenvalues (say, λ_1) of $L(j\omega)$ is zero. For the three other eigenvalues, the following ($(i) - (iii)$) should hold true:

- (i) Their product should be non-negative. Observe from (40), $\lambda_2\lambda_3\lambda_4 = -\ell_{44}|\ell_{23}|^2 - \ell_{44}|\ell_{12}|^2$. Therefore, this imposes the necessary condition that $\ell_{44} \leqslant 0$.
- (ii) Also, the sum of the products of λ_i taken two at a time should be non-negative. From (40), $\lambda_2\lambda_3 + \lambda_3\lambda_4 + \lambda_2\lambda_4 = \ell_{22}\ell_{44} - |\ell_{12}|^2 - |\ell_{23}|^2$. Observe that, for a non-zero real power transfer through the HVdc-link in the steady-state, $I^0_{d_r} \neq 0$. Therefore, from proposition 1 (see, Appendix C), $|\ell_{23}|^2 > 0$. Further, from (i) we have $\ell_{44} \leqslant 0$. These together[6], imposes the necessary condition that, $\ell_{22} < 0$ and $\ell_{44} < 0$.
- (iii) Finally, their sum should also be non-negative. From (40), this imposes the necessary condition that $\lambda_2 + \lambda_3 + \lambda_4 = \ell_{22} + \ell_{44} \geqslant 0$.

Clearly, the necessary conditions from (i) and (ii) contradict that in (iii). Therefore, $L(j\omega)$ is not positive semidefinite, and as a consequence, $G(s)$ is not positive real. This concludes the proof. □

[6] For $\ell_{44} < 0$ and $|\ell_{23}|^2 > 0$, $(ii) \implies \ell_{22} < 0$. For $\ell_{44} = 0$ and $|\ell_{23}|^2 > 0$, (ii) will clearly not hold true.

Theorem 1. (Main Result) *A VSC-HVdc system operating at unity power factor in steady state, with constant real power control, constant dc-link voltage control, and ac voltage–reactive power droop control is a source of oscillation energy.*

Proof. Observe from Lemma 1, the transfer function matrix $G(s)$ between the input-output pair u and y is not positive real. Following which, from [34, Lemma 10], it can be said that the system Ω (linearized representation of the VSC-HVdc system with these controls) is not passive with respect to the supply rate $u^T y$. This implies, the integral $\int_0^{\mathcal{T}} u^T y\ dt < 0$. And therefore, the system is a source of oscillation energy. This concludes the proof. □

Remark 1: Constant reactive power control at the rectifier and the inverter (i.e., $\Delta Q_r^{\text{ref}} = \Delta Q_i^{\text{ref}} = 0$ or in other words, $K_{q_r} = K_{q_i} = 0$) is a special case of the system description in Section II and Theorem 6.1. Therefore, a VSC-HVdc system operating at unity power factor in steady state, with constant real and reactive power control and constant dc-link voltage control is also a source of oscillation energy.

Remark 2: Please note that in this paper the oscillation source behavior of VSC-HVdc is studied only for low-frequency electromechanical oscillations ($0.2 - 2$ Hz). The averaged model discussed in deriving the mathematical results and the simplifications made may not hold true for analyzing oscillations outside this range. Therefore, it should be highlighted that the applicability of the Theorem 1 is restricted to electromechanical oscillations and should not be extended to subsynchronous oscillations (SSOs). The analysis of DEF for higher frequency oscillations (e.g. SSOs) requires detailed electromagnetic transients (EMT) modeling of the system. EMT modeling is outside the scope of this paper. Interested readers may take a look at the following research papers [26], [35], [36] and [37].

Remark 3: Inclusion of an additional modulating control on real power set point P_r^{ref}, for example – a feedback control for power oscillation damping, may transform the VSC-HVdc from a source to a sink of oscillation energy. In that case, with a suitable choice of feedback control parameters, $G(s)$ can be made positive real. Although intuitive, a detailed analytical proof may be necessary to strengthen the claim. This may be a potential topic for future research.

V. Case Studies

In this section, in support of the claims made in Theorem 1, we present case studies from the IEEE $2-$area $4-$machine and $16-$machine $68-$bus test systems. The positive-sequence fundamental-frequency phasor models of the test systems are considered for transient stability simulation. The differential-algebraic equations describing the system are coded in MATLAB and numerical simulation is performed using off-the-self solvers.

A. IEEE $2-$area $4-$machine Test System

The IEEE $2-$area $4-$machine test system from [1] is modified to include a VSC-HVdc link connecting buses 7 and

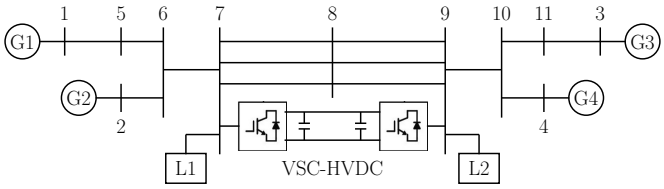

Fig. 10: Single-line diagram of the modified 2−area 4−machine system with a VSC-HVdc line between buses 7 and 9.

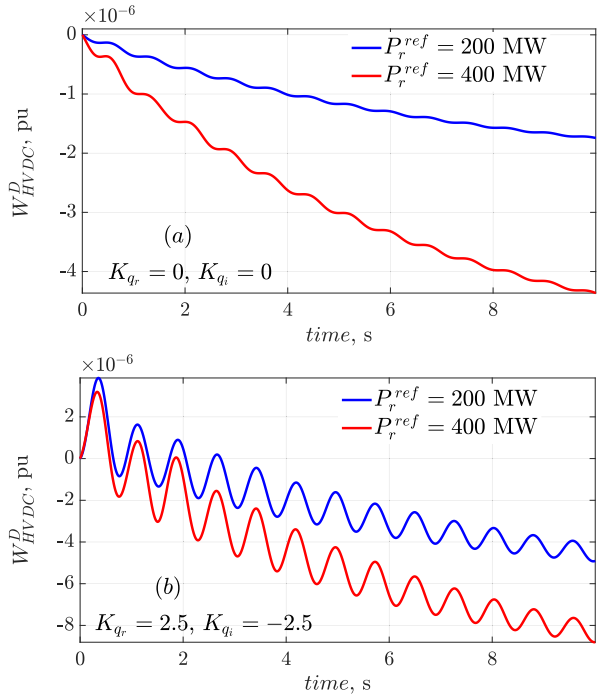

Fig. 11: Total DEF into the VSC-HVdc system for pulse disturbance in the 4−machine system with (a) constant Q^{ref} and (b) ac voltage−reactive power droop, and different P^{ref} and unity power factor in steady-state.

9 (see, Fig 10) with the controls described in Section II. The transfer functions of the proportional intergal (PI) controllers are as follows: $K_r(s) = K_v(s) = 1 + 10/s$. The detailed model of the PLL in Fig. 4 is used in the simulation with $K_{p_{\text{PLL}}} = 20$ and $K_{i_{\text{PLL}}} = 200$. For synchronuous generators, their sixth-order subtransient models are considered along with DC1A exciters and automatic voltage regulators (AVRs).

In this study, we consider two operating cases: (i) when $P_r^{\text{ref}} = 200$ MW, and (ii) when $P_r^{\text{ref}} = 400$ MW. For each of these two cases, we consider two subcases: (a) constant reactive power control at both ends[7] i.e., $K_{q_r} = K_{q_i} = 0$, and (b) ac voltage-reactive power droop control[8] with $K_{q_r} = 2.5$ and $K_{q_i} = -2.5$. Note that, in (b), the signs of the droop coefficients are opposite because in the system description (see, Section II) the directions of Q_r and Q_i are taken opposite − inward in the rectifier and outward in the inverter.

1) Verification Under Small Disturbance: A 0.1 s duration pulse disturbance is applied to the mechanical power input (P_m) of generators. The measurement signals

[7] with unity power factor in steady-state, i.e., $Q_r^{\text{ref}} = Q_r^0 = 0$ and $Q_i^{\text{ref}} = Q_i^0 = 0$.

[8] again, unity power factor in steady-state, i.e., $Q_r^{\text{ref}} = 0 + \Delta Q_r^{\text{ref}} = K_{q_r}\Delta V_{d_r}$ and $Q_i^{\text{ref}} = 0 + \Delta Q_i^{\text{ref}} = K_{q_i}\Delta V_{d_i}$.

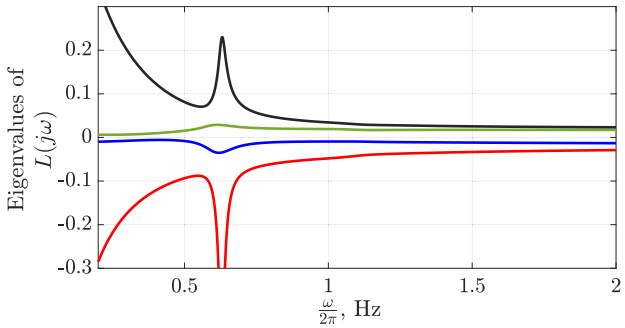

Fig. 12: Eigenvalues of $L(j\omega) = G(j\omega) + G^T(-j\omega)$ in the electromechanical oscillation range for the 4−machine system with $P_r^{ref} = 200$ MW, $K_{q_r} = 2.5$, $K_{q_i} = -2.5$.

$P_r, P_i, Q_r, Q_i, V_r, V_i, \theta_r$, and θ_i thus obtained, are detrended and filtered for the 0.65 Hz inter-area mode. Thereafter, W^D_{HVdc} – the total DEF into the HVdc system adding both the rectifier and inverter injections, is calculated (see, (49) and Fig. 20). For details on how W^D_{HVdc} is computed from these terminal measurements, please refer to Appendix D. The time domain plots of W^D_{HVdc} for different values of P_r^{ref} and droop coefficients K_{q_r} and K_{q_i} are shown in Figs 11 (a) and (b). Observe, in each case, the average slope of W^D_{HVdc} is negative, implying that the HVdc system with these controls is injecting oscillation energy into the ac network. This supports our claim in Theorem 1.

The eigenvalues of $L(j\omega) = G(j\omega)+G^T(-j\omega)$ for the case $P_r^{\text{ref}} = 200$ MW, $Q_r^0 = 0$, and $K_{q_r} = 2.5$ and $K_{q_i} = -2.5$, in the electromechanical oscillation range $0.2 - 2$ Hz, is shown in Fig. 12. Clearly, one eigenvalue is always negative. This confirms that $L(j\omega)$ is not positive semi-definite and $G(j\omega)$ is not positive real, as claimed in Lemma 1.

2) Verification Under Large Disturbance: Next, we verify the claim in Theorem 1 for large disturbances. To that end, a three-phase self-clearing fault is simulated near bus 8. The time-domain plots of the measurement signals from the rectifier and inverter terminals are shown in Fig. 21 of Appendix D. These signals are detrended and filtered for the inter-area mode and thereafter, the DEF is computed (see, Fig. 20). The DEF plots for two different droop settings are presented in Figs. 13 (a) and (b). Observe that the average slope of W^D_{HVdc} is negative supporting the claim that the VSC-HVdc is a source of oscillation energy. The DEF into the generators G1 – G4 for the case (b) are also shown in Fig. 14 for comparison. The average slopes of W^D_{Gen} for all 4 generators are positive indicating that the generators, in this case, are acting as sinks to absorb the transient oscillation energy emanating from the VSC-HVdc source.

3) Consistency with Eigenvalue Analysis: To support the conclusions of DEF-based source characterization, the following approach using eigenvalue analysis is adopted. First, we consider the base case – i.e., the IEEE 4-machine system without the HVdc. The eigenvalues and the damping ratio for the inter-area mode are calculated. Next, keeping the total system load and the set points of the generators same as before, the VSC-HVdc is introduced (as shown in Fig. 10) with the controls described in Section II. The eigenvalues for

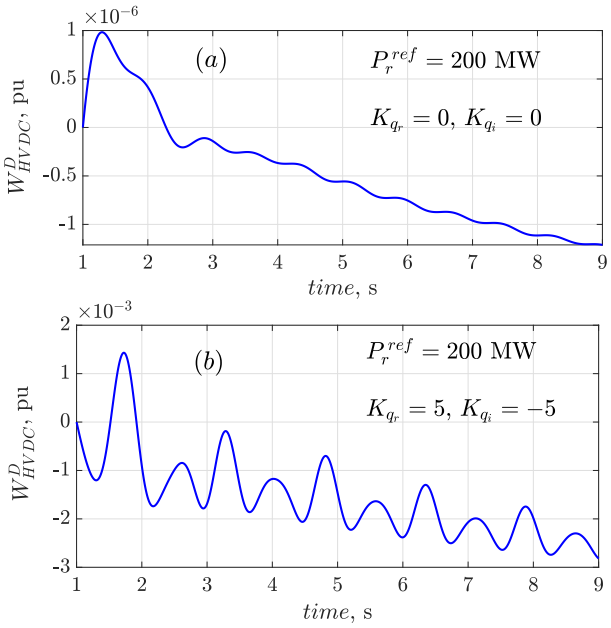

Fig. 13: Total DEF into the VSC-HVdc system following a three-phase fault in the 4−machine system with (a) constant Q^{ref} and (b) ac voltage−reactive power droop, and unity power factor in steady-state.

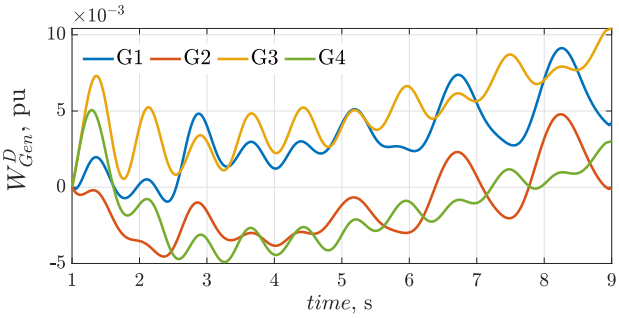

Fig. 14: DEF into the generators G1 – G4 following the three-phase fault in the 4−machine system with VSC-HVdc settings $P_r^{\text{ref}} = 200$ MW, $Q_r^0 = 0$, $Q_i^0 = 0$, and droops $K_{q_r} = 5$ and $K_{q_i} = -5$ (same as in Fig. 13(b)).

the modified system are recalculated. We know, if the VSC-HVdc is an oscillation source then the addition of it into the system should have a negative contribution to the damping, i.e., the eigenvalues for inter-area mode after inclusion of the HVdc, as compared to the base case, should shift to the right reducing the overall margin of stability. The eigenvalues in Table I supports the claim that the inclusion of the VSC-HVdc deteriorates modal damping, thereby indicating that the added device is a source of transient energy aiding in sustaining the oscillation.

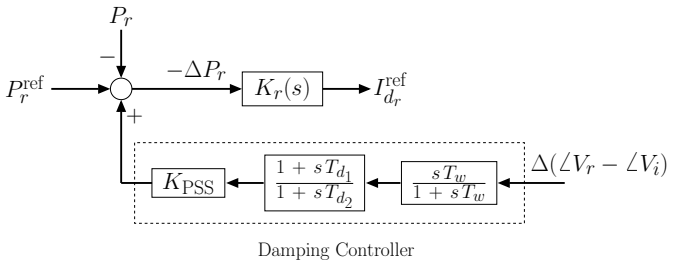

Fig. 15: Rectifier-end real power control with a supplementary damping controller modulating the power reference.

TABLE I: EIGEN-ANALYSIS OF THE IEEE 4−MACHINE SYSTEM

Case	Eigenvalues (inter-area mode)	Modal Frequency	Damping
Base Case *without* VSC-HVdc	$-0.21 \pm j3.92$	0.624 Hz	5.4%
Modified System *with* VSC-HVdc ($P_r^{\text{ref}} = 200$ MW, $K_{q_r} = 5$, $K_{q_i} = -5$)	$-0.06 \pm j3.97$	0.633 Hz	1.7%

TABLE II: EIGEN-ANALYSIS OF THE IEEE 4−MACHINE SYSTEM

Case	Eigenvalues (inter-area mode)	Modal Frequency	Damping
Modified System *with* VSC-HVdc *and* Damping Controller ($P_r^{\text{ref}} = 200$ MW, $K_{q_r} = 5$, $K_{q_i} = -5$, $K_{\text{PSS}} = 13043$, $T_{d_1} = 0.0133$ s, $T_{d_2} = 4.479$ s)	$-0.46 \pm j4.07$	0.648 Hz	11.2%

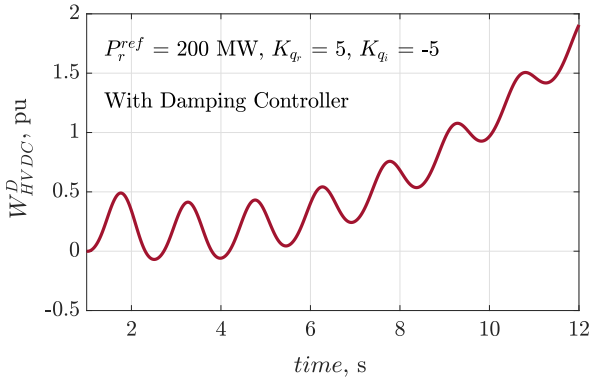

Fig. 16: Total DEF into the VSC-HVdc system following a three-phase fault in the 4−machine system in presence of a damping controller modulating the reference to the real power control.

4) Addition of a Damping Controller in the Rectifier-end Real Power Control: In Remark 3, it was hypothesized that the inclusion of a power oscillation damping control modulating the real power reference could transform the behavior of the VSC-HVdc from source to sink of oscillation energy. To confirm this, the following study is performed. The real power control in Fig. 5 is modified to include a damping controller as shown in Fig. 15. The phase angle difference between the rectifier and inverter buses is the input to the controller. In this study, the VSC-HVdc is operating with $P_r^{\text{ref}} = 200$ MW, $Q_r^0 = Q_i^0 = 0$, and droop coefficients $K_{q_r} = 5$ and $K_{q_i} = -5$. The output of the damping controller can be seen as a modulation of the real power setpoint over over its steady-state value P_r^{ref}. The damping controller parameters: the gain $K_{\text{PSS}} = 13043$, the lead-lag compensator time-constants $T_{d_1} = 0.0133$ s and $T_{d_2} = 4.479$ s, and the washout filter time-constant $T_w = 10$ s, are designed [1] to achieve the desired

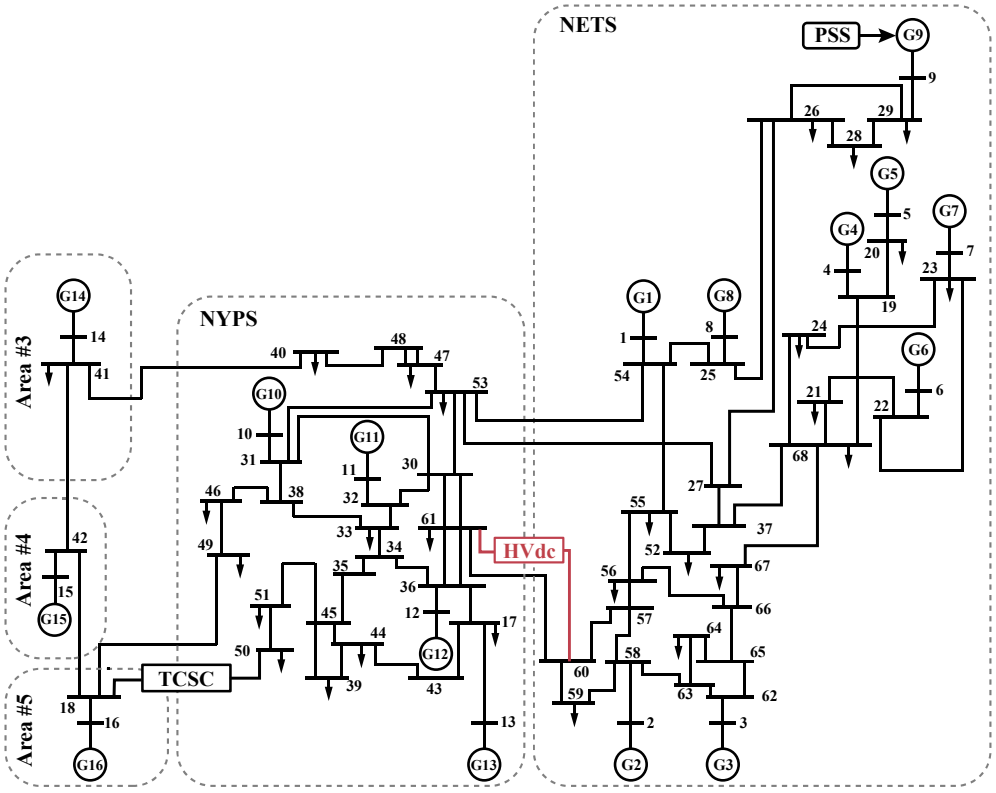

Fig. 17: Single-line diagram of the modified IEEE 16−machine 68−bus test system with a VSC-HVdc line between buses 60 and 61.

pole-placement for enhancing the damping of the inter-area mode. The eigenvalues of the system before and after addition of the damping controller are shown in the Tables I and II respectively.

To study the DEF of the modified system, a three-phase self-clearing fault is simulated near bus 8, as before. The measurement signals obtained from the rectifier and inverter-end buses are detrended and filtered. The total DEF flow into the VSC-HVdc computed from these measurements is shown in the Fig. 16. The positive slope of the W_{HVdc} confirms that the HVdc with the added damping control is acting a sink of oscillation energy. This characterization is also consistent with improvement in the damping ratio obtained from eigenvalue analysis (see, Tables I and II).

B. IEEE 16−machine 68−bus NY-NE Test System

Next, for confirming our claims, the IEEE 16-machine 68-bus NY-NE Test System [38], as shown in Fig. 17, is studied. The fundamental-frequency phasor model of the system with subtransient synchronous generator models, exciters (DC1A at G1–G8; ST1A at G9; manual excitation at G10–G16), automatic voltage regulators, and a power system stabilizer (at G9) is considered. The test system is modified to include a VSC-HVdc link connecting buses 60 and 61, with the controls described in Section II (see, Fig. 17). The PLL as shown in Fig. 4 is included. Bus 61 is operating as the inverter-station and bus 60 as the rectifier-station with $P_r^{\text{ref}} = P_r^0 = 200$ MW, $Q_r^{\text{ref}} = Q_r^0 = 0$, $Q_i^{\text{ref}} = Q_i^0 = 0$, and droop coefficients− in case (a): $K_{q_r} = K_{q_i} = 0$ and case (b): $K_{q_r} = 5$ and $K_{q_i} = -5$.

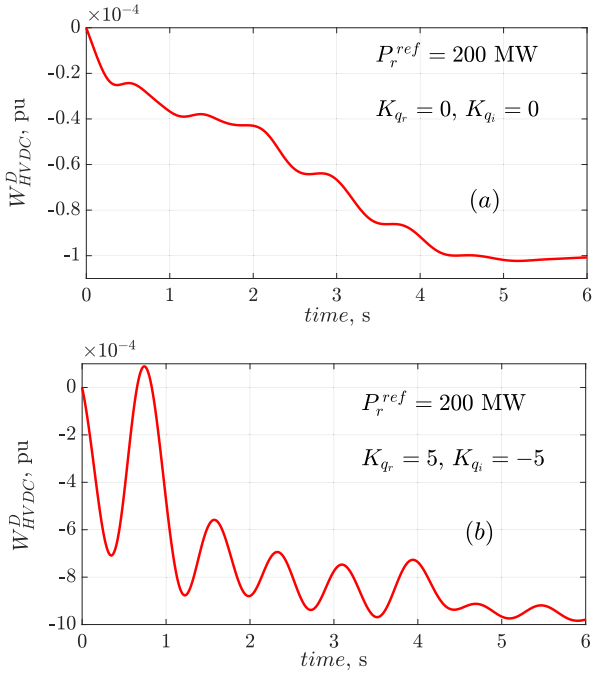

Fig. 18: Total DEF into the VSC-HVdc system for a pulse disturbance in the 16−machine system with (a) constant Q^{ref} and (b) ac voltage−reactive power droop, and unity power factor in steady-state.

A 0.2 s pulse disturbance is applied to the P_r^{ref}. The output variables are filtered for the 0.54 Hz inter-area mode. The total DEF into the HVdc system for a system mode computed for both cases (a) and (b) are shown in Figs 18 (a) and (b). Observe, for both cases (a) and (b), the average slope of

W^D_{HVdc} is negative, confirming our claim in Theorem 1 that the system can be source of oscillation energy. The DEFs into the generators for the case (b) are shown in Fig. 19 for comparison. In this case, G14, G15, and G16 are the sinks for the oscillation energy produced by the VSC-HVdc and other generators. Further observe, the negative slope of W^D_{HVdc} in Fig 18 (b) is greater than any of the generators G1 – G13.

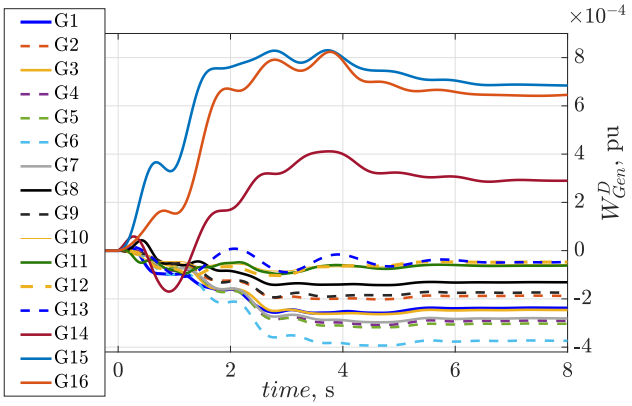

Fig. 19: DEF into the generators G1 – G16 for a pulse disturbance in the 16−machine system, with VSC-HVdc settings $P_r^{\text{ref}} = 200$ MW, $Q_r^0 = 0$, and droops $K_{q_r} = 5$ and $K_{q_i} = -5$ (same as in Fig. 18(b)).

VI. Conclusions

In this paper, analytical insights were developed into the dissipating energy based source characterization of a VSC-HVdc system for low-frequency electromechanical oscillations. The results from passivity and positive realness were used to mathematically explain why a VSC-HVdc system operating at unity power factor with constant real power control, constant dc-link voltage control, and ac voltage–reactive power droop control is a source of oscillation energy. Through this rigorous mathematical justification, the paper strengthens the understanding of oscillation energy flow in converter-interfaced transmission systems.

Appendix A
Expressions of functions $f_1(s)$, $f_2(s)$, and $f_3(s)$

$$f_1(s) = \left(sC_rV^0_{dc_r} + i^0_{dc}\right)^{-1} i^0_{dc} \tag{41}$$

$$f_2(s) = (V^0_{dc_i})^{-1}(sC_rV^0_{dc_r} + i^0_{dc})^{-1} \cdot \left\{sC_rV^0_{dc_r}(V^0_{dc_i} + 2\ i^0_{dc}R - V^0_{dc_r}) \ + \ (V^0_{dc_i} + 2\ i^0_{dc}R)i^0_{dc}\right\} \tag{42}$$

$$f_3(s) = \frac{1+s\tau_c}{2V^0_{dc_i}K_v(s)}\Big\{sC_i(V^0_{dc_i} + 2i^0_{dc}R) - 2(i^0_{dc})^2R(V^0_{dc_i})^{-1} - sC_r(V^0_{dc_r})^2(V^0_{dc_i})^{-1}(sC_iV^0_{dc_i} - i^0_{dc})(sC_rV^0_{dc_r} + i^0_{dc})^{-1}\Big\} \tag{43}$$

Appendix B
Derivation of Transfer Function $G(s)$

Following (33) and (34),

$$\{\mathcal{M}(s)\}^{-1} = \begin{bmatrix} \frac{1}{\alpha_2(s)} & 0 & 0 & 0 \\ 0 & \frac{1}{V^0_r} & 0 & 0 \\ \frac{V^0_r}{V^0_i\ \alpha_1(s)\ \alpha_2(s)} & 0 & \frac{-1}{V^0_i\ \alpha_1(s)} & 0 \\ 0 & 0 & 0 & \frac{1}{V^0_i} \end{bmatrix} \tag{44}$$

$$\{\mathcal{M}(s)\}^{-1}\ \mathcal{N}(s) = \begin{bmatrix} -\frac{I^0_{d_r}}{\alpha_2(s)} & 0 & 0 & 0 \\ -\frac{K_{q_r}}{(1+s\tau_c)\ V^0_r} & \frac{I^0_{d_r}}{V^0_r} & 0 & 0 \\ \frac{I^0_{d_r}}{\alpha_1(s)V^0_i}\left(1 - \frac{V^0_r}{\alpha_2(s)}\right) & 0 & -\frac{I^0_{d_i}}{V^0_i} & 0 \\ 0 & 0 & -\frac{K_{q_i}}{(1+s\tau_c)\ V^0_i} & \frac{I^0_{d_i}}{V^0_i} \end{bmatrix} \tag{45}$$

$$G(s) = \{\mathcal{M}(s)\}^{-1}\ \mathcal{N}(s)\ \cdot \begin{bmatrix} 0 & -\frac{1}{s} & 0 & 0 \\ \frac{1}{s} & 0 & 0 & 0 \\ 0 & 0 & 0 & \frac{1}{s} \\ 0 & 0 & -\frac{1}{s} & 0 \end{bmatrix}$$

$$= \begin{bmatrix} 0 & \frac{I^0_{d_r}}{s\ \alpha_2(s)} & 0 & 0 \\ \frac{I^0_{d_r}}{s\ V^0_r} & \frac{K_{q_r}}{s\ (1+s\tau_c)\ V^0_r} & 0 & 0 \\ 0 & \frac{-I^0_{d_r}}{s\ \alpha_1(s)V^0_i}\left(1 - \frac{V^0_r}{\alpha_2(s)}\right) & 0 & \frac{-I^0_{d_i}}{s\ V^0_i} \\ 0 & 0 & \frac{-I^0_{d_i}}{s\ V^0_i} & \frac{-K_{q_i}}{s\ (1+s\tau_c)\ V^0_i} \end{bmatrix}. \tag{46}$$

Appendix C
Proof of Proposition I

Proposition 1. For $I^0_{d_r} \neq 0$, $|\ell_{23}|^2 > 0$.

Proof. $|\ell_{23}|^2 = \frac{(I^0_{dr})^2}{\omega^2\ (V^0_i)^2\ |\alpha_1(j\omega)|^2}\left|1 - \frac{V^0_r}{\alpha_2(j\omega)}\right|^2$. Also, $1 - \frac{V^0_r}{\alpha_2(j\omega)} = \frac{1+j\omega\tau_c}{V^0_rK_r(j\omega)+j\omega\tau_c+1}$, where $K_r(s) = K_{rP} + \frac{K_{rI}}{s}$. Therefore, $\left|1 - \frac{V^0_r}{\alpha_2(j\omega)}\right|^2 = \frac{\omega^2(1+\omega^2\tau_c^2)}{\omega^2(V^0_rK_{rP}+1)^2\ +\ (V^0_rK_{rI}-\omega^2\tau_c)^2}$. Hence, $\forall\ \omega \neq 0$, $\left|1 - \frac{V^0_r}{\alpha_2(j\omega)}\right|^2 > 0 \implies$ for $I_{d_r} \neq 0$, $|\ell_{23}|^2 > 0$.

Appendix D

A. Calculation of DEF from Terminal Measurements

In the simulations of Section V, DEF flowing into the VSC-HVdc is calculated using the terminal measurements from its rectifier- and inverter-end buses.

Please refer to [12, Eqn. (16)] where it is shown that the transient energy flowing into a device $\mathcal{E}$ connected to the power network at bus ℓ can be expressed as,

$$W_{\mathcal{E}} = \int \Im\{\vec{I}^*_{inj}\ d\vec{V}_\ell\} = \int P_{inj}\ d\theta_\ell + \int Q_{inj}\ \frac{dV_\ell}{V_\ell}. \tag{46}$$

P_{inj} and Q_{inj} are respectively the real and reactive power injected *into* the device, and θ_ℓ is the bus voltage angle at

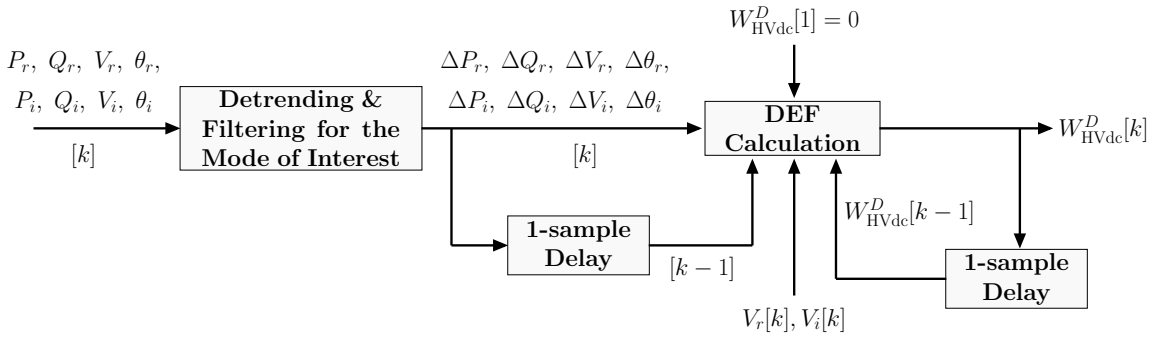

Fig. 20: Calculation of DEF from terminal measurements

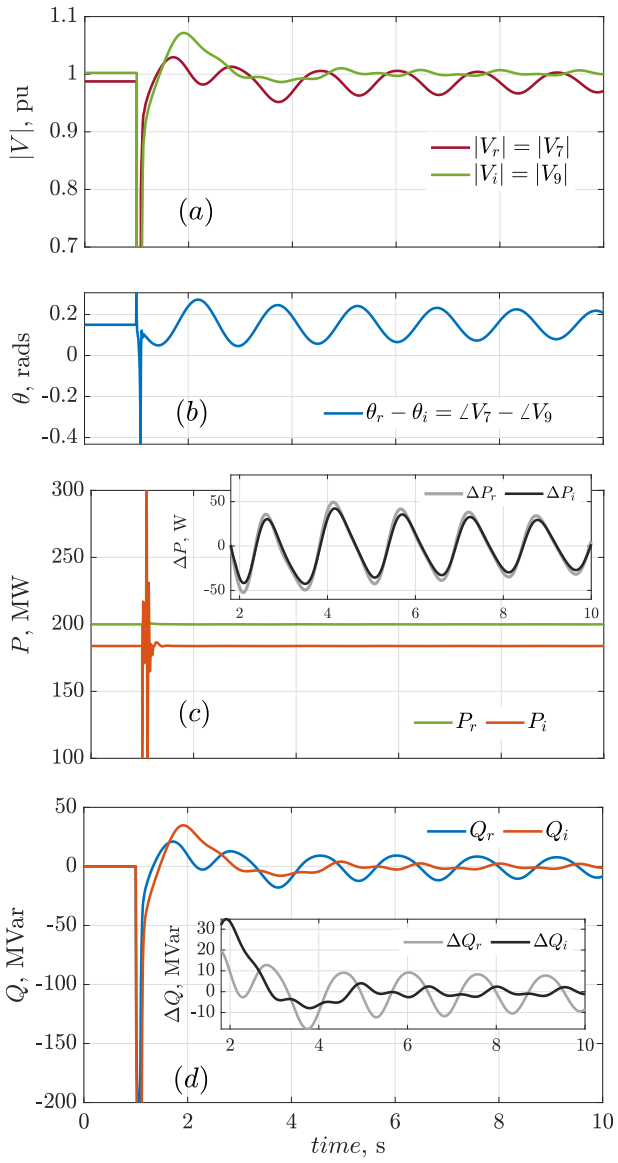

Fig. 21: Measurement signals (a) bus voltage magnitude, (b) relative bus voltage angle, (c) real, and (d) reactive powers at rectifier- and inverter-end buses (7 and 9 respectively) for a large disturbance (three-phase self-clearing fault near bus 8) in the IEEE 4-machine system. Detrended signals are shown in inset.

node ℓ. Following which, the dissipative part $W^D_{\mathcal{E}}$, can be expressed as [12, Eqn. (17)].

$$W^D_{\mathcal{E}} = \int \Delta P_{inj}\ d\Delta\theta_\ell + \int \Delta Q_{inj}\ \frac{d\Delta V_\ell}{V_\ell}. \tag{47}$$

For details on the derivation, please refer to [29, Eqns. (1)−(4)].

Extending this to the VSC-HVdc system in Section II, we can write

$$\begin{aligned} W^D_{\text{HVdc}} &= W^D_{into\ \text{rectifier}} + W^D_{into\ \text{inverter}} \\ &= \int \Delta P_r\ d\Delta\theta_r + \int \Delta Q_r\ \frac{d\Delta V_r}{V_r} \\ &- \int \Delta P_i\ d\Delta\theta_i\ -\ \int \Delta Q_i\ \frac{d\Delta V_i}{V_i}. \end{aligned} \tag{48}$$

Discretizing (48) we obtain,

$$\begin{aligned} W^D_{\text{HVdc}}[k] = W^D_{\text{HVdc}}[k-1]\ &+\ \Delta P_r[k]\ \Big(\Delta\theta_r[k] - \Delta\theta_r[k-1]\Big) \\ &+\ \Delta Q_r[k]\ \frac{\Delta V_r[k] - \Delta V_r[k-1]}{V_r[k]} \\ &-\ \Delta P_i[k]\ \Big(\Delta\theta_i[k] - \Delta\theta_i[k-1]\Big) \\ &-\ \Delta Q_i[k]\frac{\Delta V_i[k] - \Delta V_i[k-1]}{V_i[k]} \end{aligned} \tag{49}$$

where k is the sample number. The time-domain plots of the DEFs in Section V are obtained following the process described in the schematic of Fig. 20. Equation (49) is used for the DEF calculation. For initialization, we choose $W^D_{\text{HVdc}}[1] = 0$. The Δ variables in (49) are the detrended measurements bandpass-filtered for the modal frequency of interest.

B. Simulation Results for Three-phase Fault in Section V

Time-domain plots of the measurement signals for the large-disturbance case in Section V-A are shown in Fig. 21.

REFERENCES

[1] P. Kundur, *Power System Stability and Control*. McGraw-Hill, 1994.
[2] P. W. Sauer and M. A. Pai, *Power System Dynamics and Stability*. Prentice Hall, 1998.
[3] S. A. Nezam Sarmadi, V. Venkatasubramanian, and A. Salazar, "Analysis of November 29, 2005 Western American Oscillation Event," *IEEE Trans. Power Syst.*, vol. 31, no. 6, pp. 5210–5211, 2016.

[4] S. Maslennikov, B. Wang, and E. Litvinov, "Dissipating Energy Flow Method for Locating the Source of Sustained Oscillations," *Int. J. Electr Power Energy Syst.*, vol. 88, pp. 55–62, 2017.

[5] T. Huang, N. M. Freris, P. R. Kumar, and L. Xie, "A Synchrophasor Data-Driven Method for Forced Oscillation Localization Under Resonance Conditions," *IEEE Trans. Power Syst.*, vol. 35, no. 5, pp. 3927–3939, 2020.

[6] B. Wang and K. Sun, "Location Methods of Oscillation Sources in Power Systems: A Survey," *J. Mod. Power Syst. Clean Energy*, vol. 5, pp. 151–159, 2017.

[7] T. Surinkaew, K. Emami, R. Shah, S. Islam, and N. Mithulananthan, "Forced oscillation in power systems with converter controlled-based resources–a survey with case studies," *IEEE Access*, vol. 9, pp. 150 911–150 924, 2021.

[8] N. Al-Ashwal, D. H. Wilson, and M. Parashar, "Identifying Sources of Oscillations Using Wide Area Measurements," in *CIGRE US National Committee: 2014 Grid of the Future Symposium*, 2014, pp. 1–8.

[9] R. B. Myers and D. J. Trudnowski, "Effects of forced oscillations on spectral-based mode-shape estimation," in *2013 IEEE Power & Energy Society General Meeting*, 2013, pp. 1–6.

[10] W. M. and S. H., " An Analysis Method for Forced Power Oscillation Source Detection," *Proc. CSEE*, vol. 34, pp. 6209–6215, 2014.

[11] Y. Li, Y. Huang, J. Liu, and et. al., " Power System Oscillation Source Location Based on Damping Toruqe Analysis," *Power Syst. Protect. Control*, vol. 43, no. 14, pp. 84–91, 2015.

[12] L. Chen, Y. Min, and W. Hu, "An Energy-based Method for Location of Power System Oscillation Source," *IEEE Trans. Power Syst.*, vol. 28, no. 2, pp. 828–836, May 2013.

[13] R. Xie and D. J. Trudnowski, "Tracking the damping contribution of a power system component under ambient conditions," *IEEE Transactions on Power Systems*, vol. 33, no. 1, pp. 1116–1117, 2018.

[14] S. C. Chevalier, P. Vorobev, and K. Turitsyn, "Using effective generator impedance for forced oscillation source location," *IEEE Transactions on Power Systems*, vol. 33, no. 6, pp. 6264–6277, 2018.

[15] S. Chevalier, P. Vorobev, and K. Turitsyn, "A bayesian approach to forced oscillation source location given uncertain generator parameters," *IEEE Transactions on Power Systems*, vol. 34, no. 2, pp. 1641–1649, 2019.

[16] Y. Meng, Z. Yu, N. Lu, and D. Shi, "Time series classification for locating forced oscillation sources," *IEEE Transactions on Smart Grid*, vol. 12, no. 2, pp. 1712–1721, 2021.

[17] S. Maslennikov and E. Litvinov, "ISO New England Experience in Locating the Source of Oscillations Online," *IEEE Trans. Power Syst.*, vol. 36, no. 1, pp. 495–503, 2021.

[18] Y.-H. Moon, B.-H. Cho, Y.-H. Lee, and H.-J. Kook, "Derivation of Energy Conservation Law by Complex Line Integral for the Direct Energy Method of Power System Stability," in *Proceedings of the 38th IEEE Conference on Decision and Control (Cat. No.99CH36304)*, vol. 5, 1999, pp. 4662–4667.

[19] L. Chen, Y. Min, Y. Chen, and W. Hu, "Evaluation of Generator Damping Using Oscillation Energy Dissipation and the Connection With Modal Analysis," *IEEE Trans. Power Syst.*, vol. 29, no. 3, pp. 1393–1402, 2014.

[20] L. Chen, F. Xu, Y. Min, M. Wang, and W. Hu, "Transient Energy Dissipation of Resistances and its Effect on Power System Damping," *Int. J. Electr Power Energy Syst.*, vol. 91, pp. 201–208, 2017.

[21] S. Chevalier, P. Vorobev, and K. Turitsyn, "A Passivity Interpretation of Energy-Based Forced Oscillation Source Location Methods," *IEEE Trans. Power Syst.*, vol. 35, no. 5, pp. 3588–3602, 2020.

[22] Y. Zhi and V. Venkatasubramanian, "Analysis of Energy Flow Method for Oscillation Source Location," *IEEE Trans. Power Syst.*, vol. 36, no. 2, pp. 1338–1349, 2021.

[23] P. G. Estevez, P. Marchi, C. Galarza, and M. Elizondo, "Complex Dissipating Energy Flow Method for Forced Oscillation Source Location," *IEEE Trans. Power Syst.*, vol. 37, no. 5, pp. 4141–4144, 2022.

[24] R. Xie and D. J. Trudnowski, "Tracking the Damping Contribution of a Power System Component Under Ambient Conditions," *IEEE Trans. Power Syst.*, vol. 33, no. 1, pp. 1116–1117, 2018.

[25] R. Jha and N. Senroy, "Forced Oscillation Source Location in Power Systems using System Dissipating Energy," *IET Smart Grid*, vol. 2, no. 4, pp. 514–521,

[26] L. Fan, Z. Wang, Z. Miao, and S. Maslennikov, "Oscillation Source Detection for Inverter-Based Resources via Dissipative Energy Flow," Mar. 2023. DOI: 10.36227/techrxiv.22178966.v1.

[27] K. Chatterjee and N. R. Chaudhuri, "On the Equality of Modal Damping Power and the Average Rate of Transient Energy Dissipation in a Multimachine Power System," *IEEE Control Systems Letters*, vol. 6, pp. 1531–1536, 2022.

[28] Y. Hu, S. Bu, S. Yi, J. Zhu, J. Luo, and Y. Wei, "A Novel Energy Flow Analysis and Its Connection With Modal Analysis for Investigating Electromechanical Oscillations in Multi-Machine Power Systems," *IEEE Trans. Power Syst.*, vol. 37, no. 2, pp. 1139–1150, 2022.

[29] K. Chatterjee, S. Samanta, and N. R. Chaudhuri, "Insights Into Dissipating Energy-Based Source/Sink Characterization of TCSC and STATCOM for Low-Frequency Oscillations," *IEEE Transactions on Power Delivery*, vol. 38, no. 2, pp. 1426–1439, 2022.

[30] "HVDC Links in System Operations," European Network of Transmission System Operators for Electricity (ENTSO-E), Tech. Rep., December, 2019.

[31] A. Yazdani and R. Iravani, *Voltage-Sourced Converters in Power Systems: Modeling, Control, and Applications*. Wiley-IEEE Press, 2010.

[32] M. P. Bahrman and B. K. Johnson, "The abcs of hvdc transmission technologies," *IEEE Power and Energy Magazine*, vol. 5, no. 2, pp. 32–44, 2007.

[33] H. K. Khalil, *Nonlinear systems; 3rd ed.* Prentice-Hall, 2002.

[34] N. Kottenstette, M. J. McCourt, M. Xia, V. Gupta, and P. J. Antsaklis, "On Relationships among Passivity, Positive Realness, and Dissipativity in Linear Systems," *Automatica*, vol. 50, no. 4, pp. 1003–1016, 2014.

[35] Y. Ren, X. Wang, L. Chen, *et al.*, "Component damping evaluation in sub-synchronous oscillation based on transient energy flow method," *IET Gener. Transm. Distrib.*, vol. 14, pp. 460–469, 2019.

[36] Y. Ma, Q. Huang, Z. Zhang, X. Yang, and Y. Wang, "Subsynchronous oscillation analysis using multisynchrosqueezing transform and dissipating energy flow method," *IEEE Trans. Ind. Appl.*, vol. 58, no. 3, pp. 3134–3141, 2022.

[37] S. Dong, B. Wang, J. Tan, C. J. Kruse, B. W. Rockwell, and A. Hoke, "Analysis of November 21, 2021, Kaua'i Island Power System 18-20 Hz Oscillations," 2023. arXiv: 2301.05781 [eess.SY].

[38] N. R. Chaudhuri, "Wide-area Monitoring and Control of Future Smart Grids," Ph.D. dissertation, Imperial College, U.K., 2011.

Kaustav Chatterjee (S'19) received the M.Tech. degree in electrical engineering from the Indian Institute of Technology Bombay, India, in 2018, and the Ph.D. degree in electrical engineering from The Pennsylvania State University, USA, in 2022. Presently, he is a Staff Research Engineer with the Electricity Infrastructure and Buildings Division of the Pacific Northwest National Laboratory, Richland, USA. Previously, in 2021, he was a summer research intern with the Electric Power Research Institute, USA. His research is at the intersection of signal processing and system theory for online monitoring and estimation of power system dynamics. Broadly, he is interested in power system modeling, analysis, stability assessment, control, optimization, system identification, and other data-driven applications.

Sayan Samanta (S'19) received his B.Tech and M.Tech degrees in electrical engineering from the Indian Institute of Technology Kharagpur, India, in 2019, and the Ph.D. degree in electrical engineering from The Pennsylvania State University, USA, in 2023. His research interests include modeling, control and stability analysis of large power systems in presence of converters and synchronous machines.

Nilanjan Ray Chaudhuri (S'08-M'09-SM'16) received the Ph.D. degree in power systems from Imperial College London, London, UK in 2011. From 2005 to 2007, he worked in General Electric (GE) John F. Welch Technology Center. He came back to GE and worked in GE Global Research Center, NY, USA as a Lead Engineer during 2011 to 2014. Presently, he is an Associate Professor with the School of Electrical Engineering and Computer Science at Penn State, University Park, PA. He was an Assistant Professor with North Dakota State University, Fargo, ND, USA during 2014-2016. He is a member of the IEEE and IEEE PES. Dr. Ray Chaudhuri is the lead author of the book Multiterminal Direct Current Grids: Modeling, Analysis, and Control (Wiley/IEEE Press, 2014). Dr. Ray Chaudhuri was the recipient of the National Science Foundation Early Faculty CAREER Award in 2016 and Joel and Ruth Spira Excellence in Teaching Award in 2019.